Supplementary Information

Programming Magnetic Composites and Phase Change Materials for Multimodal Haptic Interfaces with Integrated Self-Sensing toward Adaptive and Proprioceptive Haptic Feedback

*Si Chen, Su Li, Yizong Li, Penghao Dong, and Shanshan Yao**

Table S1. Comparisons of representative multimodal and multi-DOF haptic devices.

Mechanism	Number of working modes	Mode	Degree of freedom	Size [mm]	Weight [g]	Flexibility	Stretchability	Self-sensing
Servo motor[1]	1	Skin stretch	1	35 × 35 × 5	–	X	X	O
Servo motor[2]	1	Skin stretch	1	29 × 45 × 126	115	X	X	X
Servo motor[3]	1	Skin stretch	2	–	–	X	X	X
Servo motor[4]	1	Skin stretch	2	41 × 41 × 5	–	X	X	X
Pneumatic[5]	1	Rotational shear	2	49 × 49 × 5	150	O	O	X
Servo motor[6]	2	Normal Skin stretch	3	57 × 32 × 27	35	X	X	X
Servo motor[7]	2	Normal Rotational shear	3	24 × 24 × 20	19	X	X	X
Servo motor[8]	2	Normal Rotational shear	3	93 × 110 × 43	306	X	X	X
Servo motor[9]	2	Normal Rotational shear	3	22 × 49 × 40	32	X	X	X
Servo motor[10]	2	Normal Rotational shear	3	36 x 25 x 26	13	X	X	X
Servo motor/Pneumatic[11]	2	Normal Rotational shear	3	113 × 30 (Length × Width)	82	X	X	X
Pneumatic[12]	2	Normal Rotational shear	3	30 × 30 (Length × Width)	–	X	X	X
Pneumatic[13]	2	Normal Rotational shear	2	6 × 250 × 80	26	O	O	X
Hydraulic[14]	2	Normal Skin stretch	3	12 × 12 × 2	4.3	O	O	X
DEA[15]	2	Normal Rotational shear	3	6 × 6 × 0.8	0.09	O	X	X
Pneumatic/Electromagnetic[16]	2	Normal Skin stretch	3	113 × 35 (Diameter x Height)	120	X	X	O
Electromagnetic[17]	2	Normal Rotational shear	2	8.5 × 11.7 × 10.8	–	O	X	O
Electromagnetic[18]	2	Normal Rotational shear	2	–	15	X	X	X
Electromagnetic[19]	2	Normal Skin stretch	2	7 × 29 × 20	4.3	O	X	X
Electromagnetic[20]	3	Normal Rotational shear Skin stretch	5	15 × 15 × 4	0.8	O	O	X
Electromagnetic **(This work)**	3	Normal Rotational shear Skin stretch	5	12 × 5 (Diameter x Height)	1.8	O	O	O

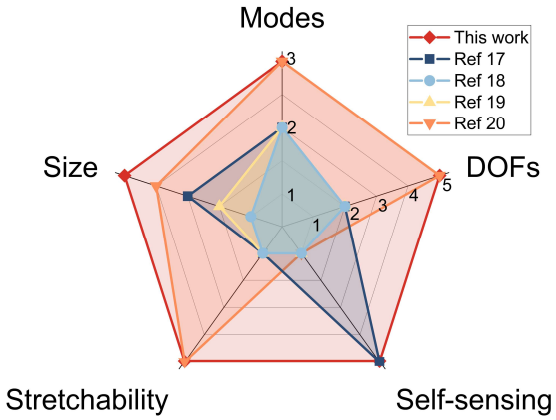

Figure S1. Comparisons of representative multimodal and multi-DOF electromagnetic actuators. For the "Modes" axis, the numeric labels represent the number of working modes. For the "Size" axis, a lower score indicates a larger device size, while a higher score corresponds to more compact form factors. For the "Stretchability" axis, a score of *1* denotes a non-stretchable design, while *5* indicates a fully stretchable design. For the "Self-sensing" axis, *1* means no self-sensing capability, and *5* indicates self-sensing integration. For the "DOFs" axis, the numeric labels represent the number of degrees of freedom.

Note S1. Mechanisms of three working modes.

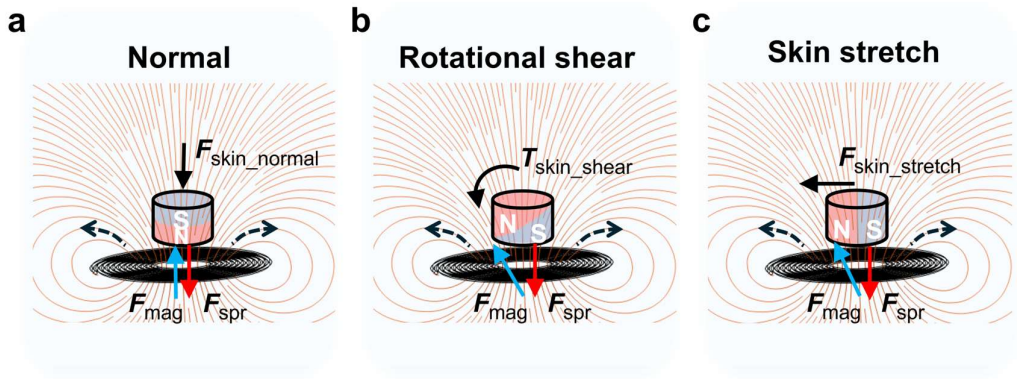

Figure S2. Force analysis diagrams of the actuator under (a) normal, (b) rotational shear, and (c) skin stretch mode.

Since the hybrid coils' magnetic field is symmetrical, the y-z plane is selected for analysis in Figure S2. For simplicity, only planar coils are shown in the schematics. Only the clockwise rotation around the x-axis ($+\Delta\theta_x$) in the rotational shear mode and the movement along the positive y-axis ($+\Delta y$) in the skin stretch mode are used as examples to explain the actuation mechanisms.

In the normal mode (Figure S2a), the soft magnet is magnetized along the z-axis ($\boldsymbol{M}$ = [0, 0, -M_z]). If the coil is energized by a counterclockwise current, the force that the soft magnet experiences can be analyzed as:

$$f(\boldsymbol{F}_{mag}, \boldsymbol{F}_{spr}, \boldsymbol{F}_{skin\_normal}, \boldsymbol{N}_{c\text{-}m}, \boldsymbol{G}) = m \cdot \ddot{\boldsymbol{s}} \quad \text{(S1)}$$

where m is the mass of the soft magnet, $\boldsymbol{s}$ is the displacement of the soft magnet from the initial position ($\boldsymbol{s} \in \mathbb{R}^3$), $\boldsymbol{F}_{skin\_normal}$ is the resistant force induced by the skin, $\boldsymbol{N}_{c\text{-}m}$ is the support force induced by the coil and applied to the soft magnet, $\boldsymbol{G}$ is the gravitational force ($\boldsymbol{N}_{c\text{-}m}$, $\boldsymbol{G} \in \mathbb{R}^3$ are hidden in the schematic illustrations for clarity), $\boldsymbol{F}_{spr}$ indicates the resistance from the RES spring ($\boldsymbol{F}_{spr} \in \mathbb{R}^3$) and its direction is opposite of the magnet's movement. Since the soft magnet is initially located at the center of the energized coil, $\boldsymbol{F}_{mag}$ acts repulsively along the z-axis, resulting in out-of-plane displacement ($+\Delta z$) of the soft magnet. Based on Newton's Third Law of Motion, in

the normal mode, the force ($\boldsymbol{F}_{\text{normal}} \in \mathbb{R}^3$) that the actuator could provide to the skin can be calculated as:

$$\boldsymbol{F}_{\text{normal}} = -\boldsymbol{F}_{\text{skin\_normal}} \tag{S2}$$

In the rotational shear mode (Figure S2b), the soft magnet is magnetized at a preset angle θ_0 (θ_0 = 45° in this work) relative to the z-axis ($\boldsymbol{M}$ = [0, -M_y, M_z]). This configuration results in a torque ($\boldsymbol{\tau}_{\text{mag}} \in \mathbb{R}^3$)[21]:

$$\boldsymbol{\tau}_{\text{mag}} = V_r \boldsymbol{M} \times \boldsymbol{B}_{\text{coil}} \tag{S3}$$

which causes the magnet to rotate about the x-axis ($\pm\Delta\theta_x$) until it reached the steady angular position ($\Delta\theta_x = \theta_0$). This resulting torque about the x-axis produces localized skin deformation through rotational shear. The force (or torque) that the soft magnet experienced can be expressed as:

$$f(\boldsymbol{\tau}_{\text{mag}}, \boldsymbol{F}_{\text{spr}}, \boldsymbol{T}_{\text{skin\_shear}}, \boldsymbol{N}_{\text{c-m}}, \boldsymbol{G}) = m \cdot \ddot{\boldsymbol{s}} \tag{S4}$$

where $\boldsymbol{T}_{\text{skin\_shear}}$ ($\boldsymbol{T}_{\text{skin\_shear}} \in \mathbb{R}^3$) indicates the torque induced by the skin.

Similarly, the torque ($\boldsymbol{T}_{\text{shear}}$) that the actuator could provide to the skin can be calculated as:

$$\boldsymbol{T}_{\text{shear}} = -\boldsymbol{T}_{\text{skin\_shear}} \tag{S5}$$

In the skin stretch mode (Figure S2c), the magnet is magnetized in-plane ($\boldsymbol{M}$ = [0, -M_y, 0]). When the coil is energized, the resulting $\boldsymbol{F}_{\text{mag}}$ induces a 90° rotation of the soft magnet, causing its edge to slide laterally across the skin surface and produce a directional skin-stretch tactile stimulus. The force experienced by the magnet can be analyzed as:

$$f(\boldsymbol{F}_{\text{mag}}, \boldsymbol{F}_{\text{spr}}, \boldsymbol{F}_{\text{skin\_stretch}}, \boldsymbol{N}_{\text{c-m}}, \boldsymbol{G}) = m \cdot \ddot{\boldsymbol{s}} \tag{S6}$$

where $\boldsymbol{F}_{\text{skin\_stretch}}$ is the frictional force induced by the interface between human skin and soft magnet ($\boldsymbol{F}_{\text{skin\_stretch}} \in \mathbb{R}^3$), and its direction opposes the motion of the soft magnet. The magnitude of $\boldsymbol{F}_{\text{skin\_stretch}}$ can be calculated as:

$$\boldsymbol{F}_{\text{skin\_stretch}} = \mu_{\text{s-m}} \cdot N_{\text{s-m}} \tag{S7}$$

$$N_{s-m} = \tau_{\text{mag}} / r_{\text{torque}} \tag{S8}$$

where $\mu_{\text{s–m}}$ is the coefficient of friction at the human skin/soft magnet interface, $N_{\text{s–m}}$ is the normal force generated by the soft magnet on the skin, and its direction is perpendicular to the skin, and r_{torque} is the radius of the rotation. In this study, $\boldsymbol{F}_{\text{skin\_stretch}}$ is obtained from direct experimental measurements. Therefore, in the skin stretch mode, the force ($\boldsymbol{F}_{\text{stretch}} \in \mathbb{R}^3$) that the actuator could provide to human skin can be obtained as:

$$\boldsymbol{F}_{\text{stretch}} = -\boldsymbol{F}_{\text{skin\_stretch}} \tag{S9}$$

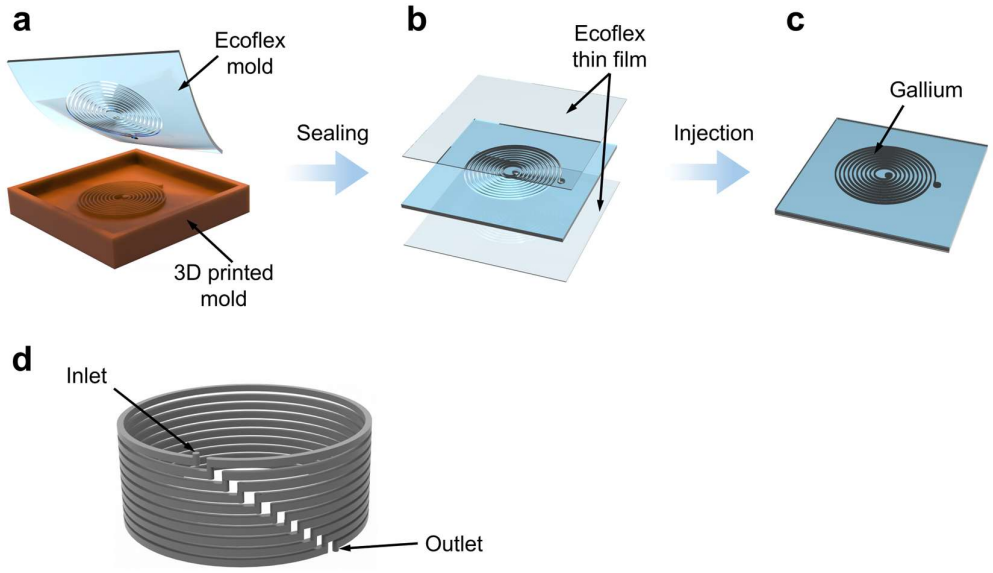

Figure S3. Schematics of the fabrication process of the gallium-based coil. (a) A single-layer Ecoflex mold with spiral microchannels is fabricated by drop-casting liquid Ecoflex into a 3D-printed template, followed by curing and peeling off the Ecoflex. (b) The patterned microchannels are sealed with Ecoflex thin film to enclose the spiral channels. (c) Liquid gallium is injected into the sealed microchannels to form a conductive, deformable planar coil. The illustrated process applies to a single-layer planar spiral coil. (d) Illustration of a gallium-based solenoid coil. For the solenoid configuration, the mold contains several single-turn channels that are stacked and connected layer by layer. For clarity, Ecoflex microchannels have been hidden. Each single-turn layer is fabricated separately using steps a-c, then aligned and bonded together to form a multilayer microchannel structure. Microchannels in each layer are connected end-to-end through vertical vias that align the start and end points, ensuring continuous flow throughout the coil. After integration, liquid gallium is injected into the connected microchannels to form a conductive, deformable solenoid coil.

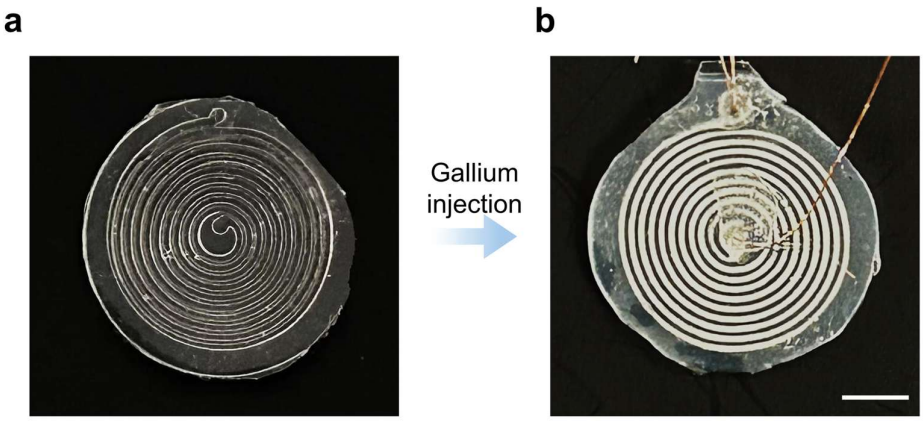

Figure S4. Photographs of the fabricated Ecoflex mold with the sealed microchannel before (a) and after (b) liquid gallium injection and lead wire connection. Scale bar: 3 mm.

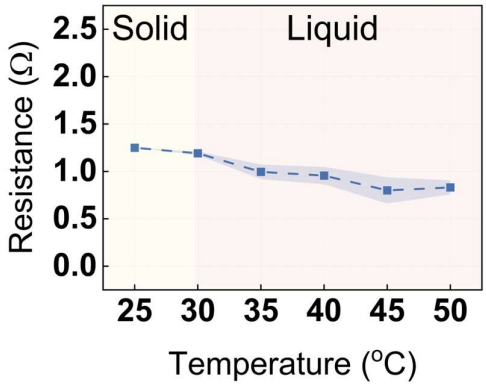

Figure S5. Resistance of the gallium-based coil as a function of temperature.

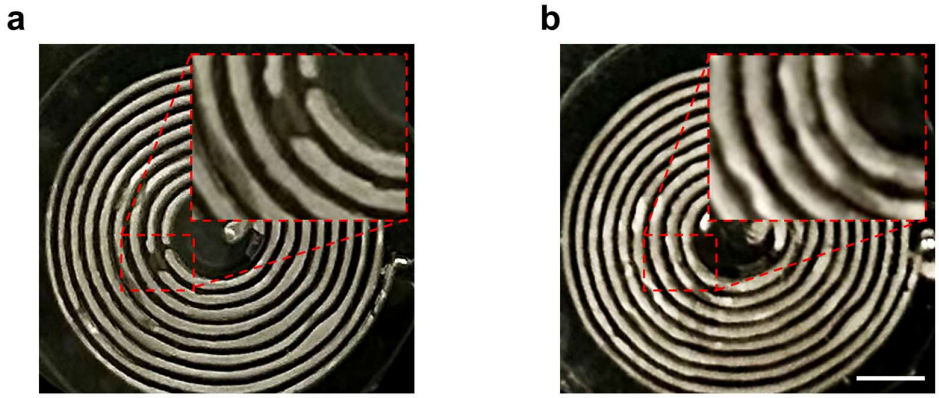

Figure S6. Self-healing behavior of the gallium-based coil (GBC). (a) Photograph of a coil showing a visible crack. GBC is in a solid state. (b) Photograph of the recovered coil after reheating at 40 °C for 30 seconds. GBC is in a liquid state. Scale bar: 2 mm.

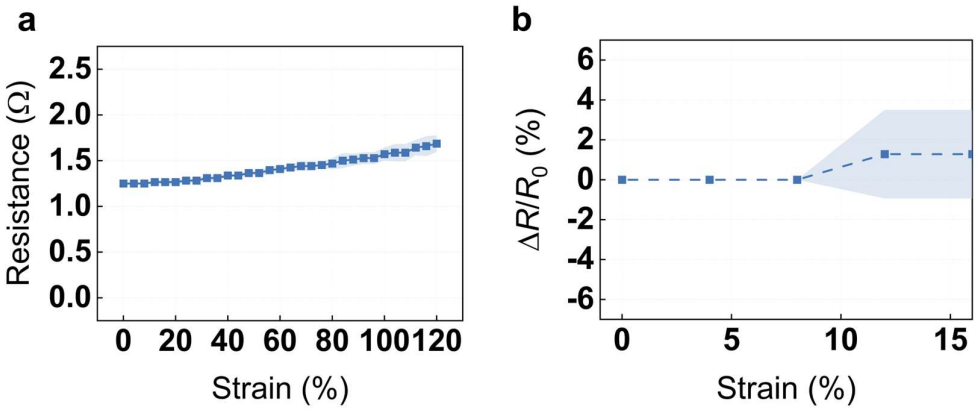

Figure S7. Electrical stability of the stretchable gallium-based coil under mechanical deformation. (a) Coil resistances as a function of the uniaxial strain up to 120%. (b) Relative resistance changes (ΔR) under 0–15 % strain, where R_0 is the initial resistance of the unstretched coil.

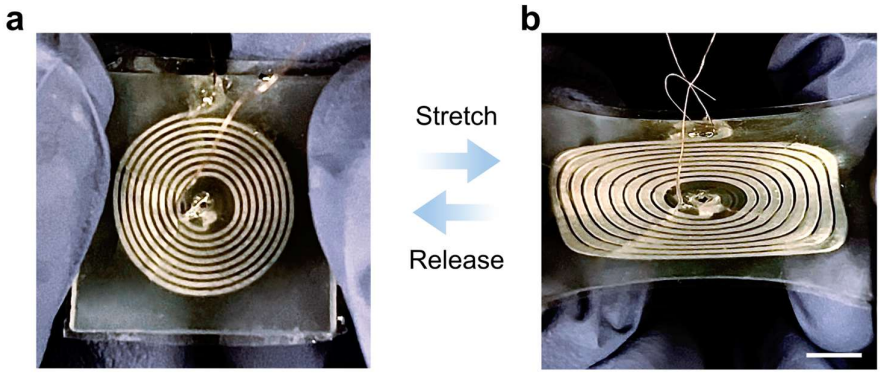

Figure S8. Stretchability of the planar gallium-based coil (GBC). (a) Optical image of the unstretched coil in its relaxed state. (b) Under uniaxial tension, the spiral coil undergoes substantial deformation while maintaining structural integrity and electrical continuity. The device returns to its original shape upon release. GBC is in a liquid state when the actuator is activated. Scale bar: 3 mm.

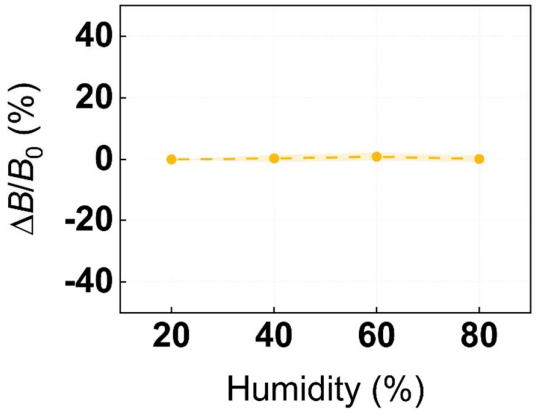

Figure S9. Magnetic flux density of the actuation coil under various humidity levels. B_0 is the magnetic flux density obtained at 20% humidity.

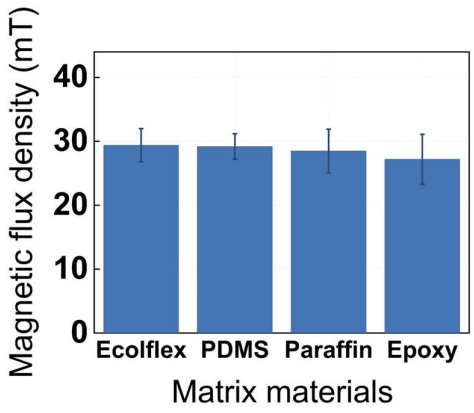

Figure S10. Magnetic flux densities of magnetic composites using different matrix materials. The weight ratio of NdFeB particles to polymer matrix is 1 : 1.

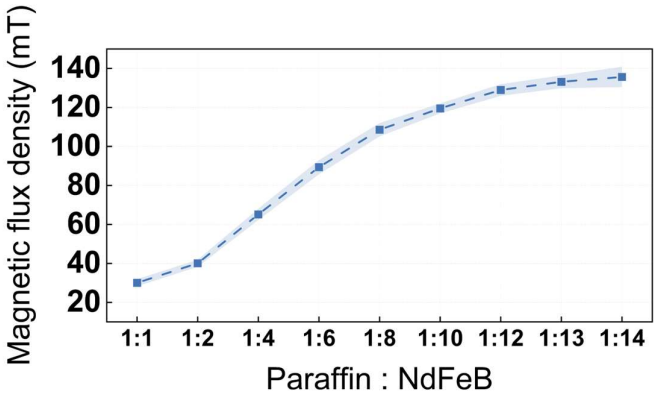

Figure S11. Magnetic flux densities of NdFeB/paraffin composites as a function of the paraffin: NdFeB weight ratio.

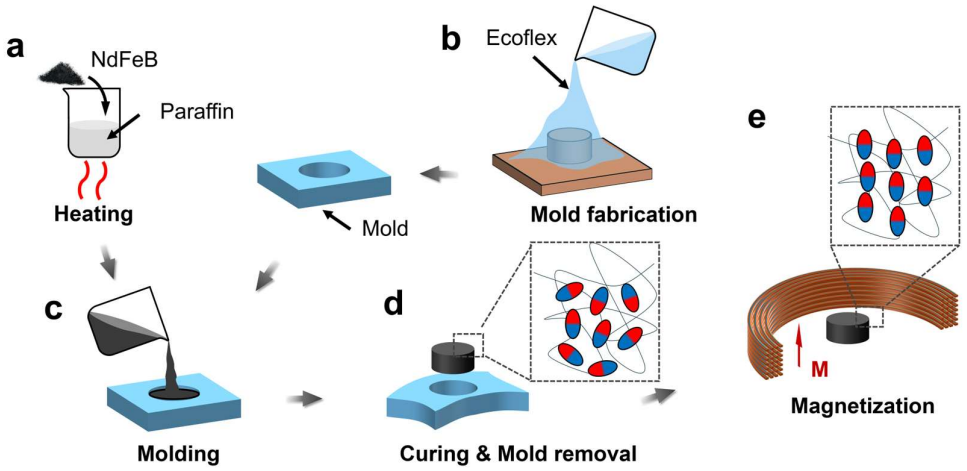

Figure S12. Schematic illustrations of the soft magnet fabrication process.

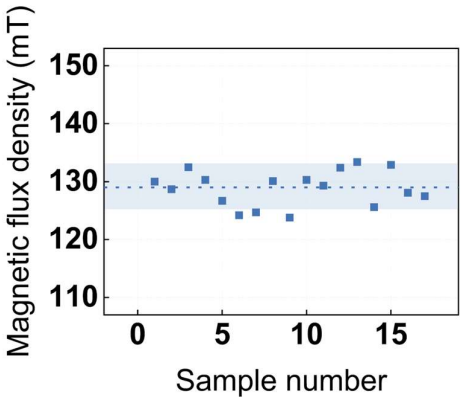

Figure S13. Magnetic flux densities measured across 16 NdFeB/paraffin composite samples (paraffin: NdFeB weight ratio = 1 : 14). The dotted line shows the mean value, and the shaded band indicates ± SD.

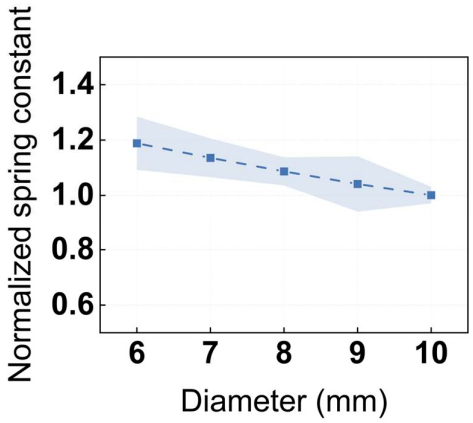

Figure S14. Normalized spring constant as a function of the RES spring outer diameter. The spring constant is normalized to the reference geometry (diameter 10 mm, cut angle 180°, 4 arms).

Note S2. Calculation of cut length

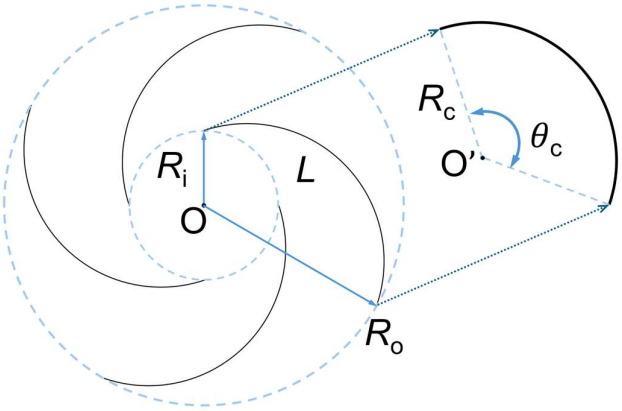

Figure S15. Schematic of the planar spiral geometry.

The cut length L of a spiral segment is calculated by approximating the arc by a cut angle θ_c and an effective radius R_c (Figure S15). The effective radius is determined as the mean of the inner radius R_i, and the outer radius R_o:

$$R_c = \frac{R_i + R_o}{2} \tag{S10}$$

The corresponding cut length is then calculated as:

$$L = \theta_c \cdot R_c \tag{S11}$$

This geometric approximation simplifies the design and analysis of the Kirigami pattern for both modeling and fabrication. The calculated values of L for different θ_c are summarized in Table S2.

Table S2. Calculated cut length (L) at various cut angles (θ_c).

θ_c (°)	60	80	100	130	150	180
L (mm)	3.44	4.48	5.78	7.21	8.70	10.21

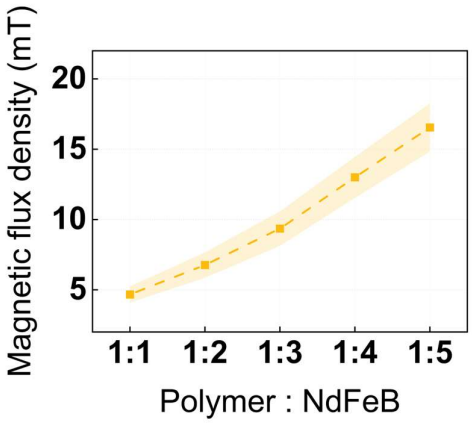

Figure S16. Magnetic flux density of the RES spring with different polymer-to-NdFeB weight ratios.

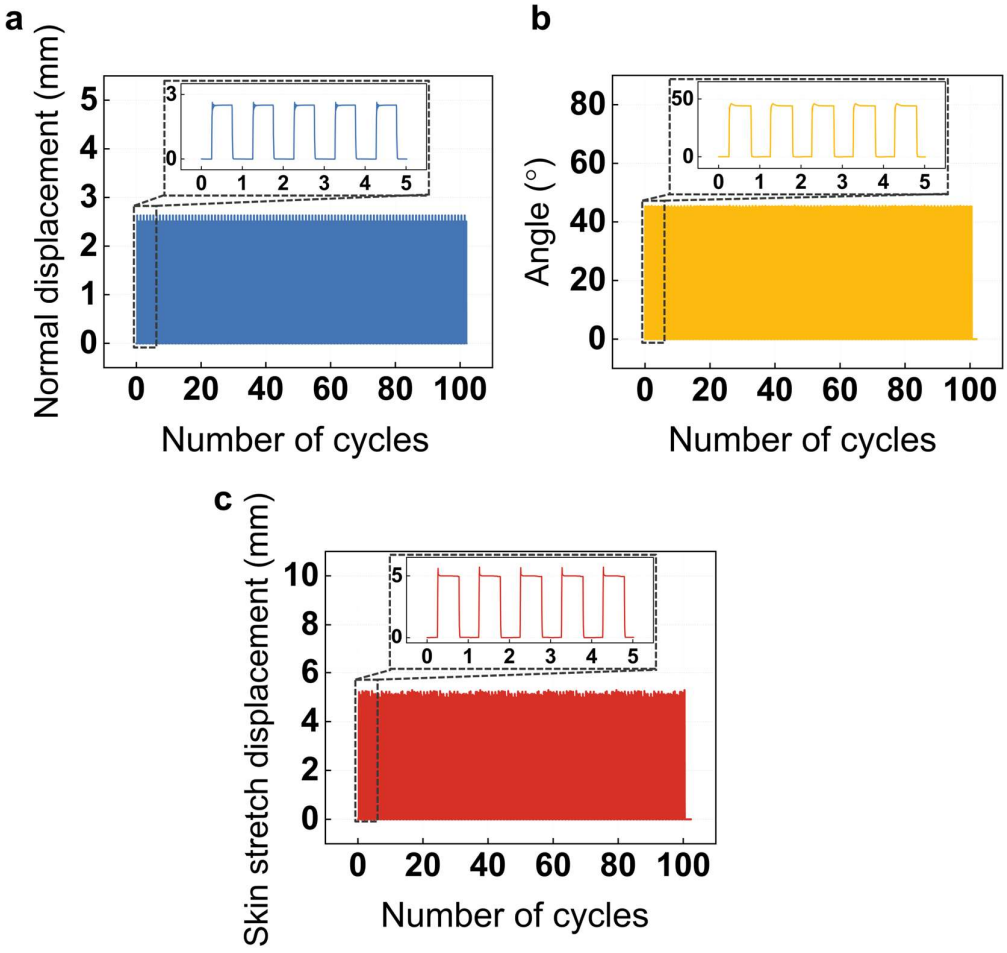

Figure S17. Cyclic testing of (a) normal, (b) rotational shear, and (c) skin stretch modes.

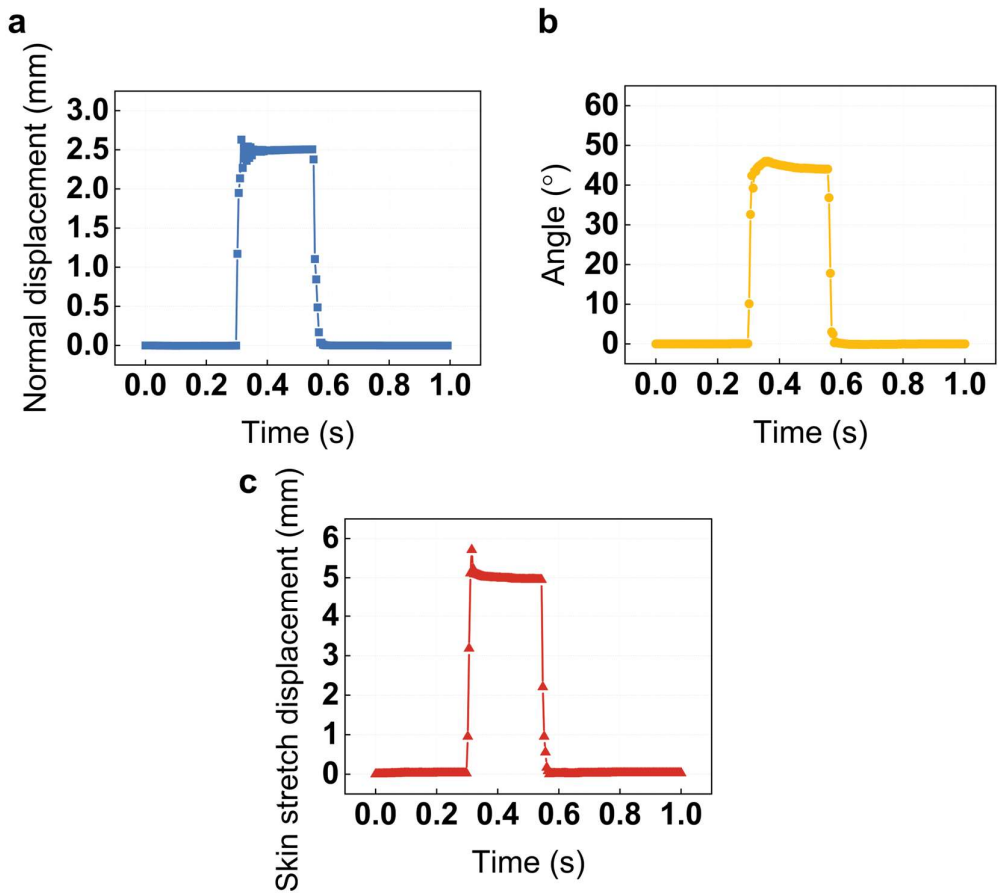

Figure S18. Response of (a) normal, (b) rotational shear, and (c) skin stretch modes. The input current is 2.4 A.

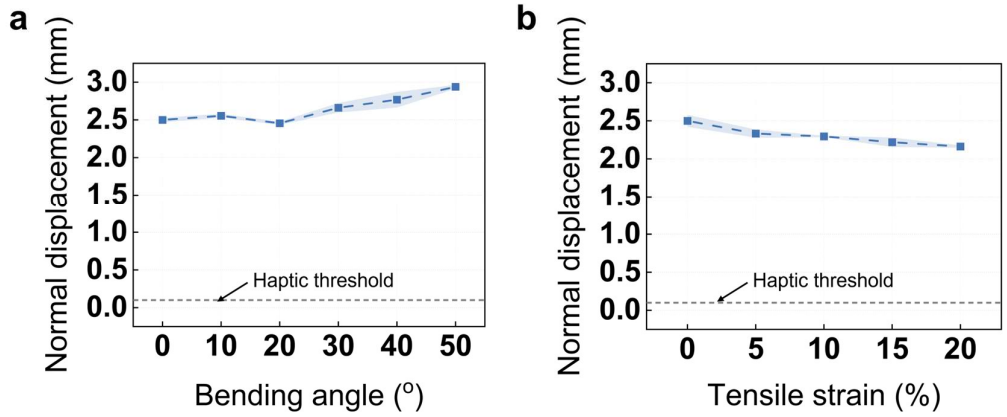

Figure S19. Performance of the actuator under (a) bending up to the fingertip curvature and (b) stretching up to the elastic strain range of the skin.

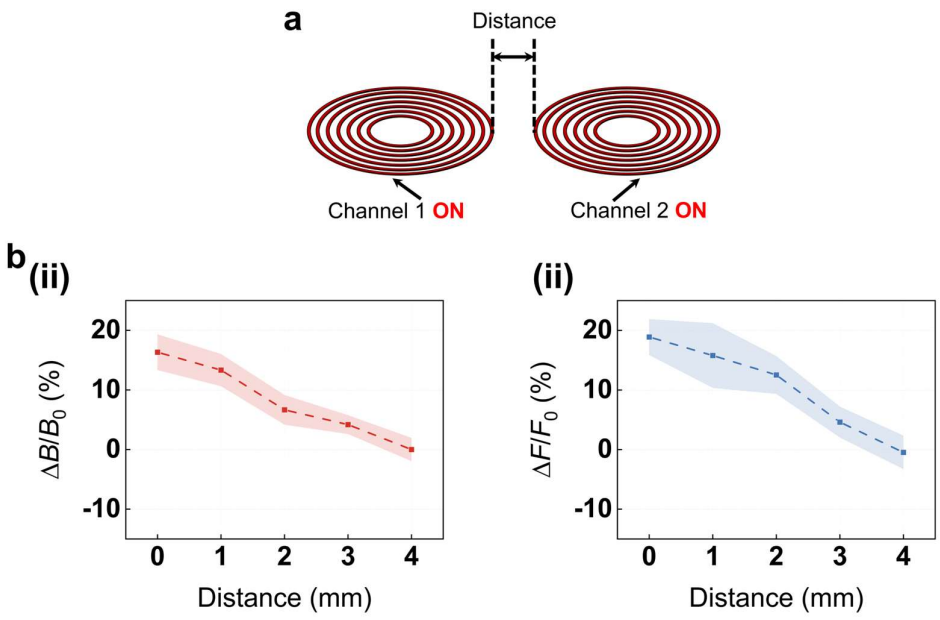

Figure S20. Channel coupling characterization for two adjacent actuation channels. (a) Schematic and (b) measured coupling when both Channel 1 and Channel 2 are ON. "Distance" represents the edge-to-edge spacing between the two channels. Coupling is quantified by the magnetic flux density and force change ratio. B_0 and F_0 are the magnetic flux density and actuation force measured at the center of Channe l when Channel 1 is energized. ΔB and ΔF are the deviation of magnetic flux density and actuation force of Channel 1 when both channels are energized.

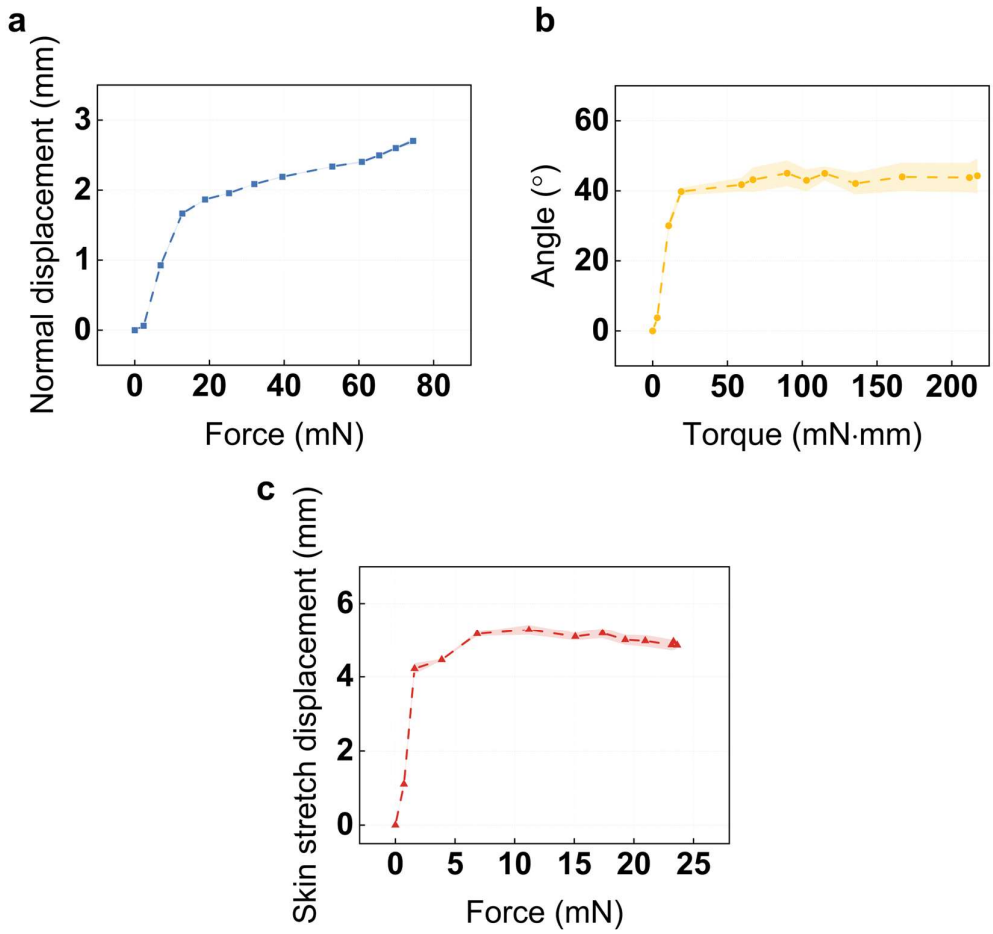

Figure S21. Displacement as a function of force in (a) normal, (b) rotational shear, and (c) skin stretch modes.

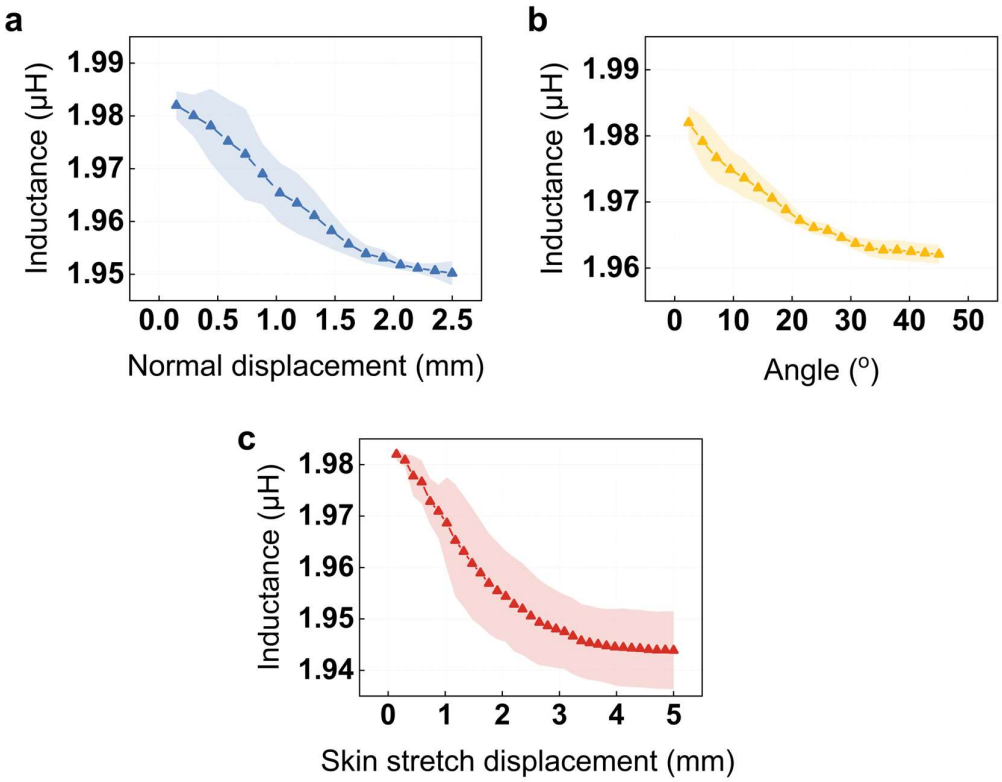

Figure S22. Inductance variations measured by the self-sensing coil during actuation in (a) normal, (b) rotational shear, and (c) skin stretch modes.

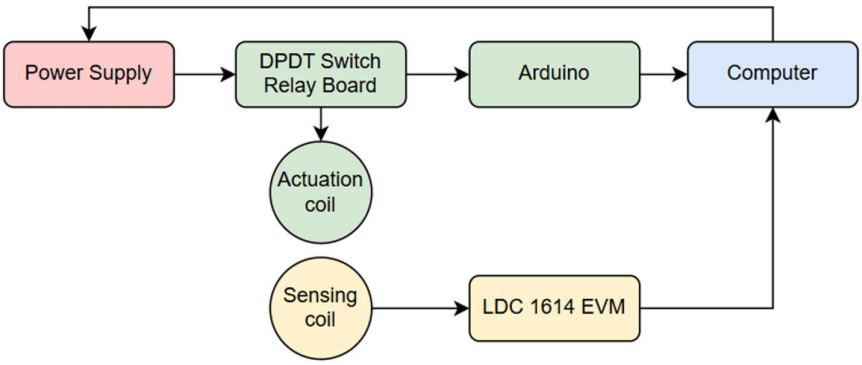

Figure S23. Schematic illustration of the control system. The actuation coil is powered by a DC power supply, with a DPDT relay board regulating the on/off state of current flow. The relay is controlled by an Arduino, which is programmed to modulate the actuation timing. At the same time, the sensing coil is connected to an LDC1614 inductance-to-digital converter to measure inductance changes in real time. The inductance changes are processed to dynamically regulate the actuation current, enabling closed-loop control.

References:

1. S. Je, B. Rooney, L. Chan and A. Bianchi, presented at Proceedings of the 2017 CHI Conference on Human Factors in Computing Systems, Denver, May, 2017.
2. K. Bark, J. W. Wheeler;, S. Premakumar; and M. R. Cutkosky., presented at Proceedings of the 2008 Symposium on Haptic Interfaces for Virtual Environment and Teleoperator Systems, Reno, March 13-14, 2008.
3. A. Manasrah and S. Alkhalil, presented at Haptics: Science, Technology, Applications: 12th International Conference, EuroHaptics 2020, Leiden, September 6-9, 2020.
4. A. Ion, E. J. Wang and P. Baudisch, presented at Proceedings of the 33rd Annual ACM Conference on Human Factors in Computing Systems, Seoul, April 18-23, 2015.
5. S. Kanjanapas, C. M. Nunez, S. R. Williams, A. M. Okamura and M. Luo, *IEEE Robot. Autom. Lett.*, 2019, **4**, 1365-1371.
6. P. Zhang, M. Kamezaki, Y. Hattori and S. Sugano, presented at 2022 International Conference on Robotics and Automation (ICRA), Philadelphia, May 23-27, 2022.
7. H. Kim, H. Yi, H. Lee and W. Lee, presented at CHI Conference on Human Factors in Computing Systems, Montreal, April 21-26, 2018.
8. L. Meli, I. Hussain, M. Aurilio, M. Malvezzi, M. K. O'Malley and D. Prattichizzo, *IEEE Robot. Autom. Lett.*, 2018, **3**, 2198-2205.
9. S. B. Schorr and A. M. Okamura, *IEEE Trans. Haptics*, 2017, **10**, 418-430.
10. F. H. Giraud, S. Joshi and J. Paik, *IEEE Trans. Haptics*, 2022, **15**, 131-141.
11. K. T. Yoshida, C. M. Nunez, S. R. Williams, A. M. Okamura and M. Luo, presented at 2019 IEEE World Haptics Conference (WHC), Tokyo, July 9-12, 2019.
12. E.-H. Lee, S.-H. Kim and K.-S. Yun, *Actuators*, 2021, **10**, 60.
13. M. Zhu, A. H. Memar, A. Gupta, M. Samad, P. Agarwal, Y. Visell, S. J. Keller and N. Colonnese, presented at Proceedings of the 2020 CHI Conference on Human Factors in Computing Systems, Honolulu, April, 2020.
14. M. T. Thai, T. T. Hoang, P. T. Phan, N. H. Lovell and T. Nho Do, *IEEE Access*, 2020, **8**, 157878-157891.
15. E. Leroy, R. Hinchet and H. Shea, *Adv. Mater.*, 2020, **32**, e2002564.
16. K. T. Yoshida, Z. A. Zook, H. Choi, M. Luo, M. K. O'Malley and A. M. Okamura, *IEEE Trans. Haptics*, 2024, **17**, 483-495.
17. M. T. Flavin, K. H. Ha, Z. Guo, S. Li, J. T. Kim, T. Saxena, D. Simatos, F. Al-Najjar, Y. Mao, S. Bandapalli, C. Fan, D. Bai, Z. Zhang, Y. Zhang, E. Flavin, K. E. Madsen, Y. Huang, L. Emu, J. Zhao, J. Y. Yoo, M. Park, J. Shin, A. G. Huang, H. S. Shin, J. E. Colgate, Y. Huang, Z. Xie, H. Jiang and J. A. Rogers, *Nature*, 2024, **635**, 345-352.
18. M. Sarac, T. M. Huh, H. Choi, M. R. Cutkosky, M. D. Luca and A. M. Okamura, *IEEE Robot. Autom. Lett.*, 2022, **7**, 6099-6106.
19. L. Fang, T. Zhu, E. Pescara, Y. Huang, Y. Zhou and M. Beigl, presented at Proceedings of the Augmented Humans International Conference 2022,

Kashiwa, March 13-15, 2022.
20. S. Chen, L. Yu, W. Shen, B. Fong, Y. Li, P. Dong, H. Qin and S. Yao, *Adv. Funct. Mater.*, 2024, **34**, 2314515.
21. R. M. Erb, J. J. Martin, R. Soheilian, C. Pan and J. R. Barber, *Adv. Funct. Mater.*, 2016, **26**, 3859-3880.